



Feasibility study of in-line particle image velocimetry

Markus Raffel¹ · Johannes N. Braukmann¹ · Christian E. Willert² · Luca Giuseppini³ · C. Christian Wolf¹

Received: 16 August 2023 / Revised: 27 November 2023 / Accepted: 10 January 2024 / Published online: 28 February 2024
© The Author(s) 2024

Abstract

This article describes recent tests and developments of imaging and evaluation techniques for particle image velocimetry (PIV) that exploit the forward scattering of tracer particles by placing the camera in-line with the illuminating light source, such as a laser or a light emitting diode. These techniques have been in use for some time in microscopy and in the design of optical instruments in astronomy. However, they have not yet been used for macroscopic PIV flow measurements. This study highlights the most promising approaches of the various recording configurations and evaluation techniques.

1 Introduction

A common method to visualize and quantify the flow field of a transparent fluid is to add small tracer particles following the local instantaneous flow field. The tracer particles are illuminated by an artificial light source such as a laser. More recently, high-power LEDs have been used for illumination, mainly in combination with larger particles in water or helium-filled soap bubbles (HFSB) in low-speed air flows. The motion of the illuminated particles is then imaged by a camera system which, after appropriate post-processing, provides a quantitative measurement of the flow velocity field. The large family of PIV implementations comprises numerous variants of this principle, utilizing different camera

setups (single camera, stereoscopic system or multi-camera system), image acquisition methods (double-frame or time-resolved recording) or modes of illumination (quasi-planar or volumetric). Closely related to PIV, methods such as particle tracking velocimetry (PTV) or “Shake-the-Box” (STB) use very similar approaches to particle imaging, but differ in their evaluation strategies. In any case, sufficient illumination of the particle images is a challenge, especially in gaseous flows. This is due to the small particle size, with particle diameters on the order of micrometers to ensure accurate flow tracking, along with short light pulses or image integration times on the order of nanoseconds to microseconds required to avoid motion blur. As a consequence, the region of interest is often limited by the available power or pulse energy of the light source. With increasing energy levels, laser safety issues have to be considered, particularly for out-of-lab applications. An example within the authors’ scope of research are full-scale flight tests, e.g., see Schwarz et al. (2022), which include routing a helicopter’s flight path through a laser light sheet. Hence, measurement techniques with a strongly reduced laser energy are preferable.

Essential for reliable PIV processing are high-contrast particle image recordings, that is, the intensity of the scattered light must be sufficiently high to be clearly distinguishable from the background. On the illumination side the resulting particle image intensity, and therefore the contrast of the PIV images, is directly proportional to the scattered light power. Rather than simply increasing the laser or light emitting diode (LED) power, it is often more effective to increase the image intensity by properly selecting the tracer particles and optimizing the optical setup.

✉ Markus Raffel
Markus.Raffel@dlr.de

Johannes N. Braukmann
Johannes.Braukmann@dlr.de

Christian E. Willert
Chris.Willert@dlr.de

Luca Giuseppini
Luca.Giuseppini@dlr.de

C. Christian Wolf
Christian.Wolf@dlr.de

¹ Institute of Aerodynamics and Flow Technology, German Aerospace Center (DLR), Bunsenstr. 10, 37073 Göttingen, Germany

² Institute of Propulsion Technology, German Aerospace Center (DLR), Linder Höhe, 51147 Cologne, Germany

³ Politecnico di Milano, Piazza Leonardo da Vinci 32, 20133 Milan, Italy

The light scattered by small particles is primarily determined by the following parameters:

- particle size and shape
- orientation of camera and light source
- ratio of the refractive indices of the particles and the surrounding medium
- light polarization
- observation angle.

For spherical tracer particles with diameters D_p larger than the wavelength λ of the incident light, Mie scattering theory can be applied. A detailed description and discussion can be found in the literature, e.g., see Bohren and Huffman (1998) or Raffel et al. (2018).

Figure 1 shows the polar distribution of the scattered light intensity for oil particles of different diameters in air with a wavelength of 532 nm according to Mie's theory. The intensity is shown on a logarithmic scale and plotted so that the value for neighboring circles differs by a factor of 100. Mie scattering can be characterized by the normalized diameter, q , given by

$$q = \frac{\pi D_p}{\lambda}. \quad (1)$$

The resulting azimuthal distribution of the scatter is complex, but the intensity is higher in the forward direction. When q is greater than one, local maxima appear in the

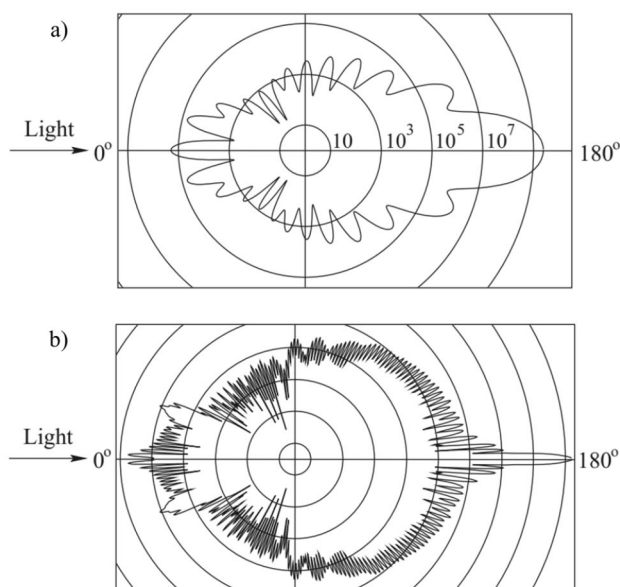


Fig. 1 Light (532nm) scattering behavior of oil particles with 1 μm (a) and 10 μm (b) in air, adapted from Raffel et al. (2018)

angular distribution. As q increases, the ratio of forward to backward scattering intensity increases rapidly.

In multi-camera setups such as stereoscopic PIV or tomographic PIV, the cameras can be arranged to take advantage of forward scattering to increase the signal in the camera images. In the case of conventional planar PIV, however, single camera imaging is most commonly performed at an observation angle of 90° to avoid perspective errors and uncertainties due to unfocused particle images resulting from the limited depth of focus of the imaging system, see Fig. 2a.

Aside from the clear tendency of the scattered light intensity to increase with increasing particle diameter, the scatter distributions in Fig. 1 illustrate that the relationship between light intensity and particle diameter is characterized by rapid oscillations, assuming that only one specific observation angle is considered.

When using a camera system with a finite aperture, rather than a hypothetical pinhole, the image of each tracer particle will include a range of slightly different viewing angles depending on the aperture and viewing distance. As a result, the intensity curve of an individual particle is greatly smoothed, reducing the effects discussed above.

The Mie scattering plots of Fig. 1 indicate that the light is not blocked by the small particles, but spreads out in all azimuthal directions. Assuming a sufficiently large number of particles in the light sheet, excessive multi-scattering occurs. In this case, the light imaged by the camera is not only due to direct scattering from the initial light source, but also due to light scattered by other particles (secondary scattering). In the case of heavily seeded flows and planar PIV, this greatly increases the intensity of individual particle images, because the intensity of the light received directly from the particle—at 90° to the incident illumination—is orders of magnitude smaller than that received via multi-scattering, which involves much stronger forward scattering. However,

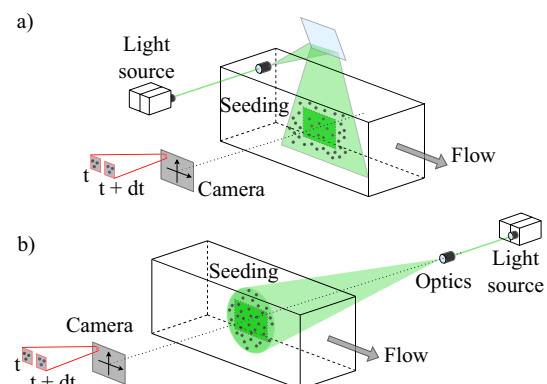


Fig. 2 Sketches of sample setups for conventional planar PIV (a) and in-line PIV (b)

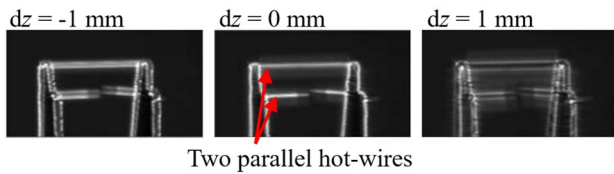


Fig. 3 Parallel hot-wire probe, two $5\ \mu\text{m}$ -wires, recorded with a lens of $f = 400\ \text{mm}$ and $f_{\#} = 2.8$ at a distance of about $1\ \text{m}$. The images show the focal plane, $dz = 0$, and out of plane positions, $dz = \{-1, 1\}\ \text{mm}$

since multi-scattering by many particles increases not only the intensity of the particle image but also that of the background image, the image contrast cannot be increased significantly and extremely high particle densities are therefore usually avoided.

The current work demonstrates the feasibility of several in-line imaging configurations and the subsequent evaluation, see Fig. 2. When the camera is placed in-line, the effective measurement volume in the direction of the line of sight is not limited by the well-defined edges of a laser light sheet or volume, but by the depth of focus (DoF) of the camera/lens combination. As an example, images of two $5\ \mu\text{m}$ hot-wires recorded with an aperture of $f_{\#} = 2.8$, see Fig. 3, the DoF is only about $2\ \text{mm}$. The DoF can also be calculated based on the approach described in the appendix. The maximum blur that is acceptable is highly dependent on the size of the spatial filter, that is used in the post processing of the images. In case of Fig. 3 the acceptable blur is around 6px which corresponds to a calculated DoF of 1.3mm .

In the literature, in-line configurations have rarely been used for PIV measurements. However, there are other fields that use somewhat similar configurations to the current work, which also provide some inspiration for the optical setup. In particular, one field where an in-line setup is widely used is dark field microscopy (DFM). This technique uses a dark-field condenser and selective illumination to achieve low image background levels and high signal-to-noise ratios. In particular, in DFM the path of the unscattered incident light is typically excluded from the detection range of the scattered signal probe, see Fig. 4a for an example.

A complete review of recent advances in this technique can be found in Gao et al. (2021), while a more specific application with a detailed setup description is presented in Wei et al. (2007). Another research area where an in-line setup is commonly used is astronomy. A typical challenge is to block out the direct light from a star or other bright objects in order to resolve nearby darker objects that would otherwise be hidden in the bright glare. To solve this problem, a coronagraph is often used, which is a special telescope arrangement, an example of which is shown in Fig. 4b. There are several ways to achieve the goal of suppressing

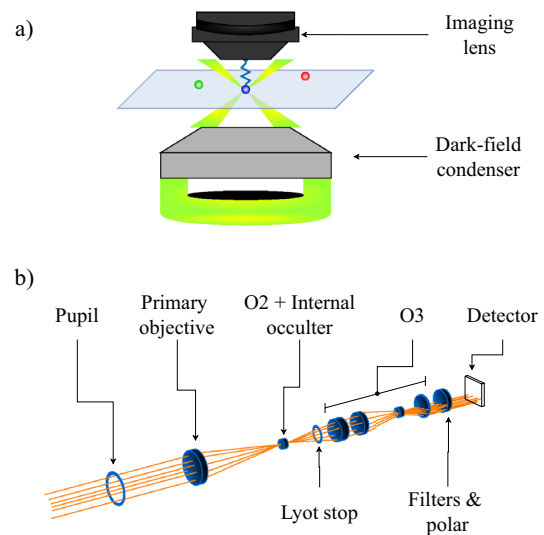


Fig. 4 Related measurement principles: **a** dark-field microscopy (DFM), and **b** optical coronagraph, adapted from Gao et al. (2021) and Renotte et al. (2015)

the bright light from a central source, for example phase masks (Rouan et al. 2000), occulting disks (Renotte et al. 2015) or adaptive optics (Jovanovic et al. 2015).

Beyond the aforementioned applications, in-line imaging arrangements are also frequently employed in various optical flow measurement techniques, most notably for digital inline holography (DIH) which is commonly used for reconstructing particle fields in multiphase flows. A recent review on this topic was compiled by Huang and Cai (2022).

The most commonly used optical in-line technique in aerodynamics is schlieren or shadow photography (Scharadin 1942). The optical setup of Toepler's schlieren method consists of spherical mirrors or lenses and a light trap, often in the form of a half aperture, e.g., a knife edge. It captures variations in light intensity proportional to the first derivative of the fluid density (Settles 2001). However, setups used for schlieren photography can also be used for in-line PIV. A setup very similar to Toepler's schlieren method was implemented within this study and is also described in the following.

2 In-line PIV configurations

2.1 Initial test with polarizing filters

The initial idea for an in-line configuration used a principle borrowed from microscopy. Two polarization filters with an offset of 90° , e.g., vertical and horizontal, were placed in the direct path between the light source and the camera to reduce the illumination intensity sufficiently, see Fig. 5. The tracer particles introduced between the two polarization filters

must be able to depolarize the incident light sufficiently to allow the scattered light to pass through the second polarization filter. Since this is not the case for very small particles ($D_p \approx 1 \mu\text{m}$) commonly used in aerodynamic PIV measurements, the experiment was performed using larger HFSB with $D_p \approx 300\text{--}400 \mu\text{m}$. The results showed the viability of this approach, even with a preliminary setup using only a flashlight (MagLite LED 3D, electrical power 0.8 W, LED chip size $1.5 \times 1.5\text{mm}$) for illumination and a mobile phone camera for imaging.

Figure 6a is a raw image showing bright tracer particles with parts of the optical setup still visible despite the polarization filter. Applying a spatial high-pass filter matched to the expected particle size helps to isolate the seeding from the optical components (see Fig. 6b). The gain in particle visibility was not satisfactory, but the result is still shown as some fluids can carry particles that are non-spherical and therefore have the potential to depolarize the scattered light to a greater extent. During the investigations it appeared that a more effective blocking of the direct light could be achieved by removing the filters and using light traps.

2.2 Setup with a light trap in front of the imaging lens

Figure 7 shows another example of an in-line PIV setup. The light from a small but intense light source is focused by an illuminating lens onto a light trap, which in this case is located in front of a distant imaging lens. The minimum required size of the light trap depends on the geometry of the light source, but is much smaller than the aperture of the imaging lens. As a result, most of the emitted light is blocked and does not reach the image sensor, but light scattered in the forward direction by the particles, as well as stray light caused by lens imperfections and lens contamination, does reach the image sensor. The imaging lens focuses the seeding within the depth of field into sharp particle images just a few pixels in diameter, while blurred particles and parasitic lens imperfections increase the overall brightness of the image.

A first impression of the working principle is given by the preliminary setup shown in Fig. 8. The light source was the

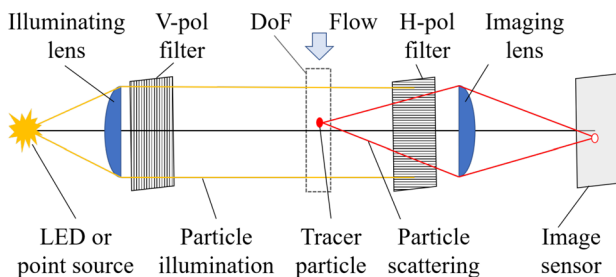


Fig. 5 Sketch of an in-line setup using two polarizing filters

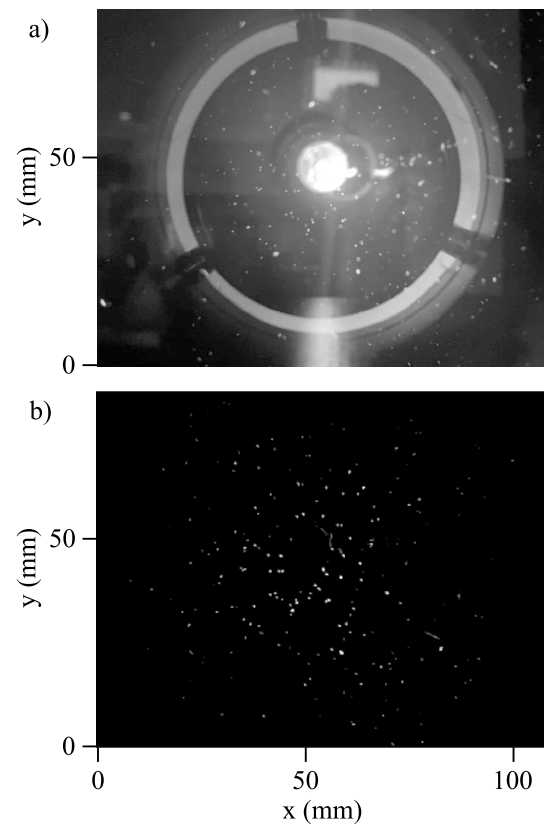


Fig. 6 Sample for in-line image acquisition with polarizing filters, raw image (a) and high-pass filtered image (b)

same as in the previous section (MagLite LED 3D), but the mobile phone camera was replaced by a Nikon D7100 DSLR camera with an image size of 4000×6000 pixels. Two identical long focal length lenses (Nikon Nikkor 400 mm, $f_\# = 2.8$) were used, one on the illumination side and one on the imaging side. The tracer particles of typically $15 \mu\text{m}$ diameter were provided by a soap bubble generator (TSI BG1000). A raw sample image is shown in Fig. 9a, which is dominated by bright cloud-like scattered light structures. Similar to the polarization setup, the tracer particles can be isolated by an appropriately chosen spatial high-pass filter

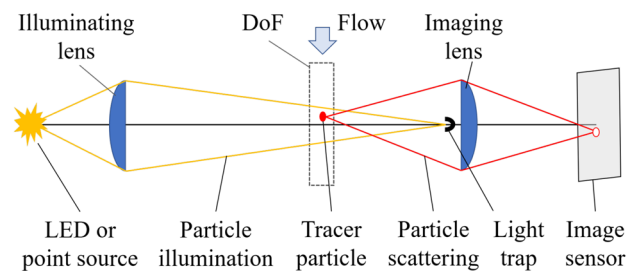


Fig. 7 Sketch of an in-line setup with a light trap in front of the imaging lens, “configuration A”

Fig. 8 Preliminary in-line setup with a light trap in front of the imaging lens

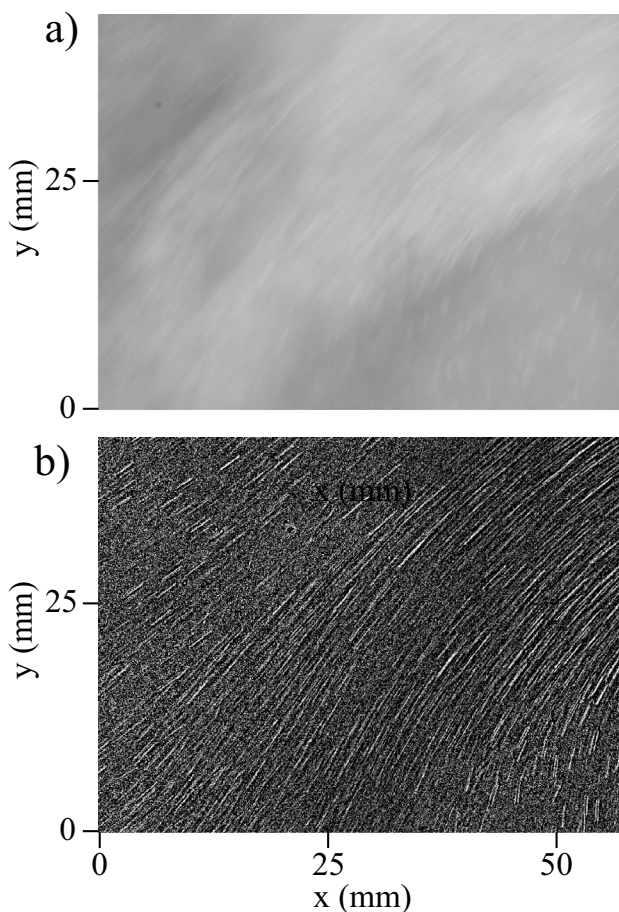
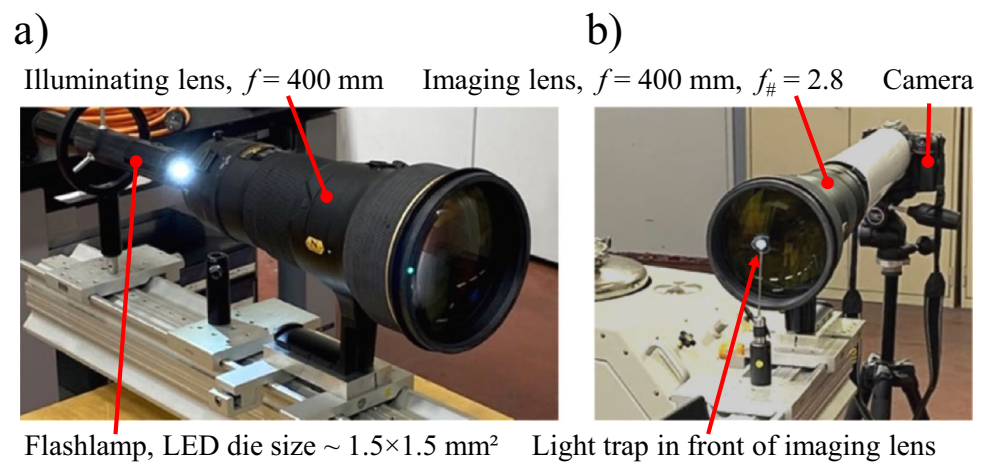


Fig. 9 In-line imaging result obtained with the preliminary setup shown in Fig. 8, raw image (a) and high-pass filtered image (b) to remove stray light

(see Fig. 9b. In this case, the low-pass filtered image (kernel size 7px) was subtracted from the original image. The contrast of the filtered image is good, but the continuous light source and the long exposure time of 1 ms leads to

particle streaks rather than sharp particle images. However, the sharpness and intensity of the streak images proved the suitability of the recording setup not only for streak velocimetry but also for PIV.

2.2.1 Bluff-body flow with pulsed LED illumination

To overcome the limitations of the preliminary setup, the configuration with a light trap in front of the imaging lens, see Fig. 7, was upgraded with a double-pulsed LED light source (Hardsoft IL-106 G) that emits green light, $\lambda = 528$ nm. The pulse duration was set to 10 μ s with a pulse energy of approximately 100 μ J. The lens system was retained from the previous setup, but the images were captured by a sCMOS double-shutter camera (PCO, Edge 5.5) with an image size of 2560 \times 2160 pixels. Image pairs were acquired at a frame rate of 5 Hz and an inter-frame/pulse separation of 20 μ s. A Seika CTS-1000 seeding device provided a dense stream of di-ethylhexyl sebacate (DEHS) tracer particles approximately $D_p = 1.5$ μ m in diameter. It should be noted that most of the hardware components for this setup are standard PIV equipment. The tracer particles were sucked through a test section by a vacuum cleaner, which also removed excess particles thereby reducing light scattering by particles outside of the measurement volume. The flow direction is perpendicular to the optical axis, and a 4 mm diameter wooden cylinder was placed at the upstream end of the measurement region to act as an obstacle to the flow. Figure 10a shows an example raw image with flow from left to right, the shear layers and the wake of the cylinder are already visible in the seeded flow. In order to obtain an image similar to standard PIV recording, a filter implemented in DaVis was used (see Fig. 10b. The chosen filtering method involved subtracting the minimum intensity value within the whole set of recorded images of each pixel. The measurement area is only about 35 \times 30 mm^a, limited by

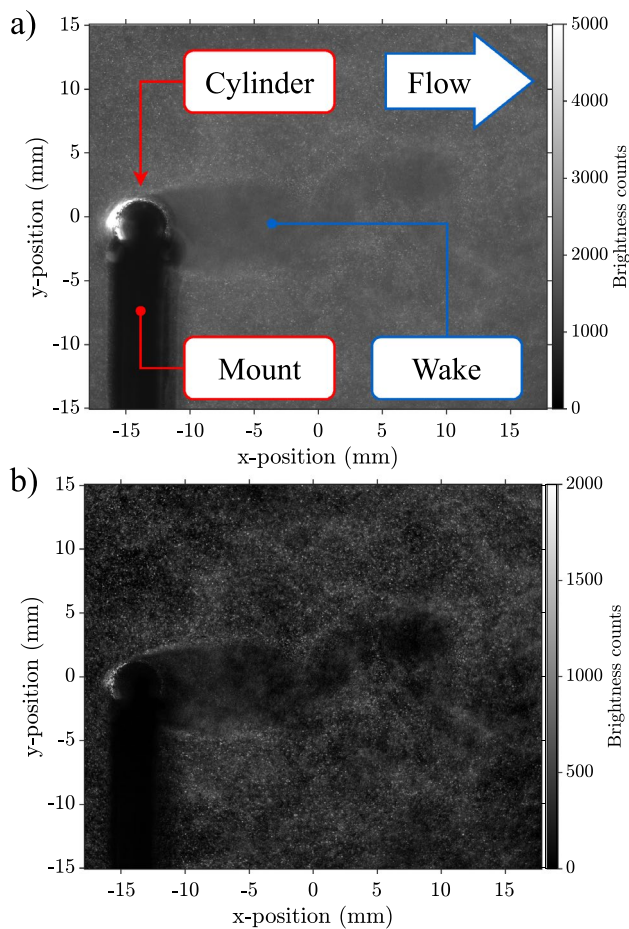


Fig. 10 Sample in-line PIV image with pulsed LED illumination, light trap in front of the imaging lens, raw image (a) and high-pass filtered image (b)

the aperture of the illuminating lens and the converging illumination cone as shown in Fig. 7.

The acquired image pairs were processed with the PIV software (LaVision DaVis 10) using an adaptive iterative cross-correlation algorithm with an initial window size of 128×128 pixels (50% overlap) and a final window size of 32×32 pixels (75% overlap). A sample result is shown in Fig. 11 using the horizontal velocity component as a scalar background (a) and the correlation coefficient (b).

The average free stream velocity is approximately 13 ms^{-1} , with the turbulent wake of the cylinder clearly visible in the center of the measurement region. Note that the vertical mounting post of the cylinder blocks the line of sight of the camera, but it is located outside the measurement region and the flow. Therefore, it does not leave a visible wake itself. The correlation value is approximately between 0.25 and 1.0, with the highest values in the external flow and the lowest values in the turbulent wake.

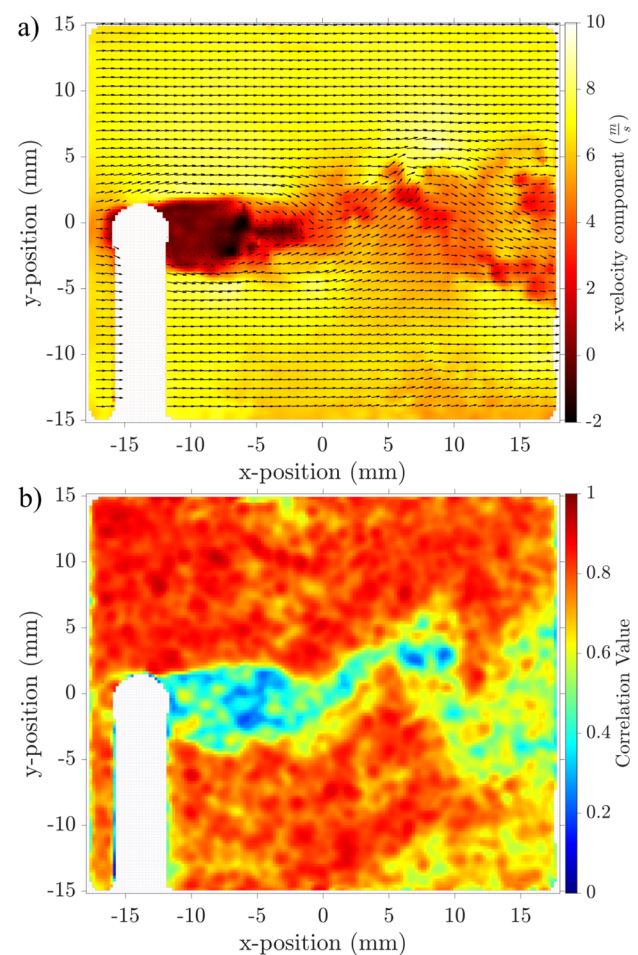


Fig. 11 Sample result for the raw image in Fig. 10, u-component velocity field (a, with every 6th vector in horizontal/vertical direction) and corresponding correlation coefficient (b)

2.2.2 Duct flow with laser illumination and high-speed camera

The experiment described next is another variant of the with a light trap in front of the imaging lens as depicted in Fig. 7. The light of a low-cost laser (NEJE Tool E30130, $\lambda = 450 \text{ nm}$, $P_{\text{cont.}} = 5.2 \text{ W}$) is expanded to about 50 mm using an $f = -30 \text{ mm}$ biconcave lens and an $f = +250 \text{ mm}$ plano-convex lens. A pair of vertical vignettes then creates an 8 mm thick light volume that is passed orthogonal through the square test section of a small wind tunnel. The illuminated volume is imaged by a high-speed CMOS camera (Vision Research V1840) fitted with an $f = 200 \text{ mm}$ macro lens (Nikon Micro Nikkor 200mm 1:4) and a $2\times$ teleconverter (Nikon TC-201). The working distance is 575mm between the plane of focus (i.e., measurement plane) and the front of the lens. With the lens aperture at $f_{\#} = 4.0$ and an image magnification of $23.6 \mu\text{m}/\text{pixel}$ ($M = 0.65$) the DoF is estimated at 0.5 – 1 mm using the equations given in the

appendix. The light is directed to the edge of the camera lens (see Fig. 12) such that the angle between optical axis and laser light amounts to about 3° . A blind on the edge of the lens reduces light scatter.

The channel has a square test section with an internal dimension of $H^2 = 76 \times 76 \text{ mm}^2$ and an overall length of 1800 mm. Measurements are performed at $x = 1700 \text{ mm}$ downstream from the 10 : 1 contraction nozzle. A tripping fence at the test section entry ensures the growth of turbulent boundary layers along the wall of the duct. For the measurements, the tunnel is operated at a bulk velocity of about 3.5 ms^{-1} . Seeding is provided globally upstream in the settling chamber and consists of $D_p \approx 1 \mu\text{m}$ paraffin droplets generated by a Laskin nozzle seeding generator (PIVTEC PivPart14).

Matching the framing rate of the high-speed camera, a pulse-width modulated laser (NEJE Tool E30130, $\lambda = 450 \text{ nm}$, $P_{\text{cont.}} = 5.2 \text{ W}$) is triggered with pulses of $2 \mu\text{s}$ duration, thereby producing light pulses with an estimated energy of $5 \mu\text{J}$ per pulse. Due to the blinds only about 20% ($1 \mu\text{J}/\text{pulse}$) is actually introduced into the test section.

Sample recordings obtained at 10 kHz are provided in Fig. 13. The leftmost image, Fig. 13a, represents the average intensity computed from a sequence of 20,000 images. Figure 13b is a combined image of five successive raw images. Subtracting the long-term average (a) removes the stationary

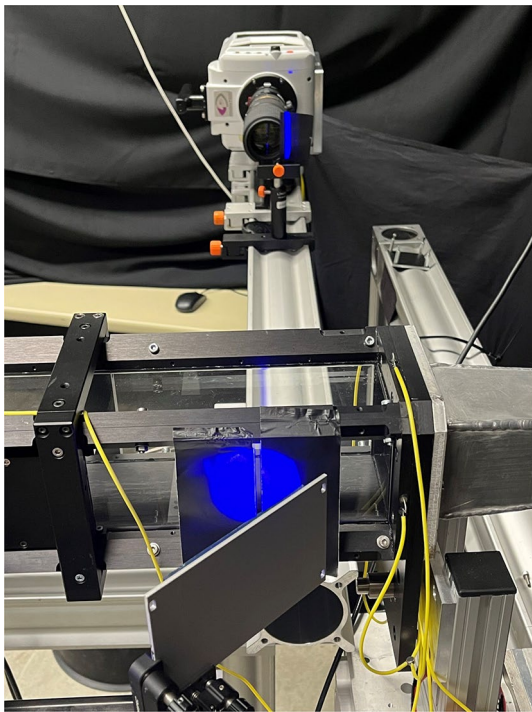


Fig. 12 Illumination setup for high-speed in-line PIV in a small square duct using a blue pulse width modulation (PWM) laser and a high-speed CMOS camera

stray light in (b), enhancing the visibility of the tracer particles in Fig. 13c. Applying an additional low-pass filter further improves the contrast of the particles while attenuating high-frequency noise that would otherwise reduce the quality of the cross-correlation processing (Fig. 13d).

Example measurements of the turbulent flow in the square duct are presented in Fig. 14. The measurement plane (e.g., plane of focus) is located near the mid-plane of the duct. The velocity profile is computed from 2 s of image data acquired at 20 kHz (40 000 images at 2048×200 pixels). Using 5 images per time-step, multi-frame PIV processing is performed with samples of 32×32 pixels ($0.75 \times 0.75 \text{ mm}^2$) at 50% overlap.

While the mean velocity profile closely matches the DNS data at similar Reynolds number (Schlatter and Örlü 2010), the variances are either over- or underestimated. In part, this can be attributed to insufficient record length of about 180 boundary layer turn-over times ($2 U_{cl}/H$). More importantly, the integration of particle image data across a depth of field covering several mm introduces noise in the correlation signal and at the same time leads to spatial smoothing of the velocity fluctuations.

2.3 Setup with a light trap between imaging lens and sensor

One of the main disadvantages of the previous configuration in Sect. 2.2 is the limited size of the measurement area, since the illumination cone converges from the aperture of the illuminating lens onto the light trap. A parallel or even divergent light cone can be facilitated by placing the beam trap behind the imaging lens rather than in front of it, see Fig. 15. This benefit comes at the cost of an increased complexity of the setup. The setup is basically similar to a simple focusing schlieren setup, but in this case, the scattered light from the particles in the focal plane is visualized rather than the spatial gradients of the refractive index.

2.3.1 Bluff-body flow with pulsed LED illumination

Except for the position of the light trap, the first test with a cylindrical bluff body uses the same setup and hardware components as described in Sect. 2.2.1. This includes the double-pulsed LED illumination, the double-shutter camera, the DEHS tracer particles and the adaptive cross-correlation algorithm used to determine the particle displacements. Figure 16 shows an example raw image (a) and its high-pass filtered counterpart (b), while Fig. 17 shows the resulting horizontal velocity component as a scalar background (a) together with the corresponding correlation coefficient (b). For a one-to-one comparison with Figs. 10 and 11, the field of view was kept constant.

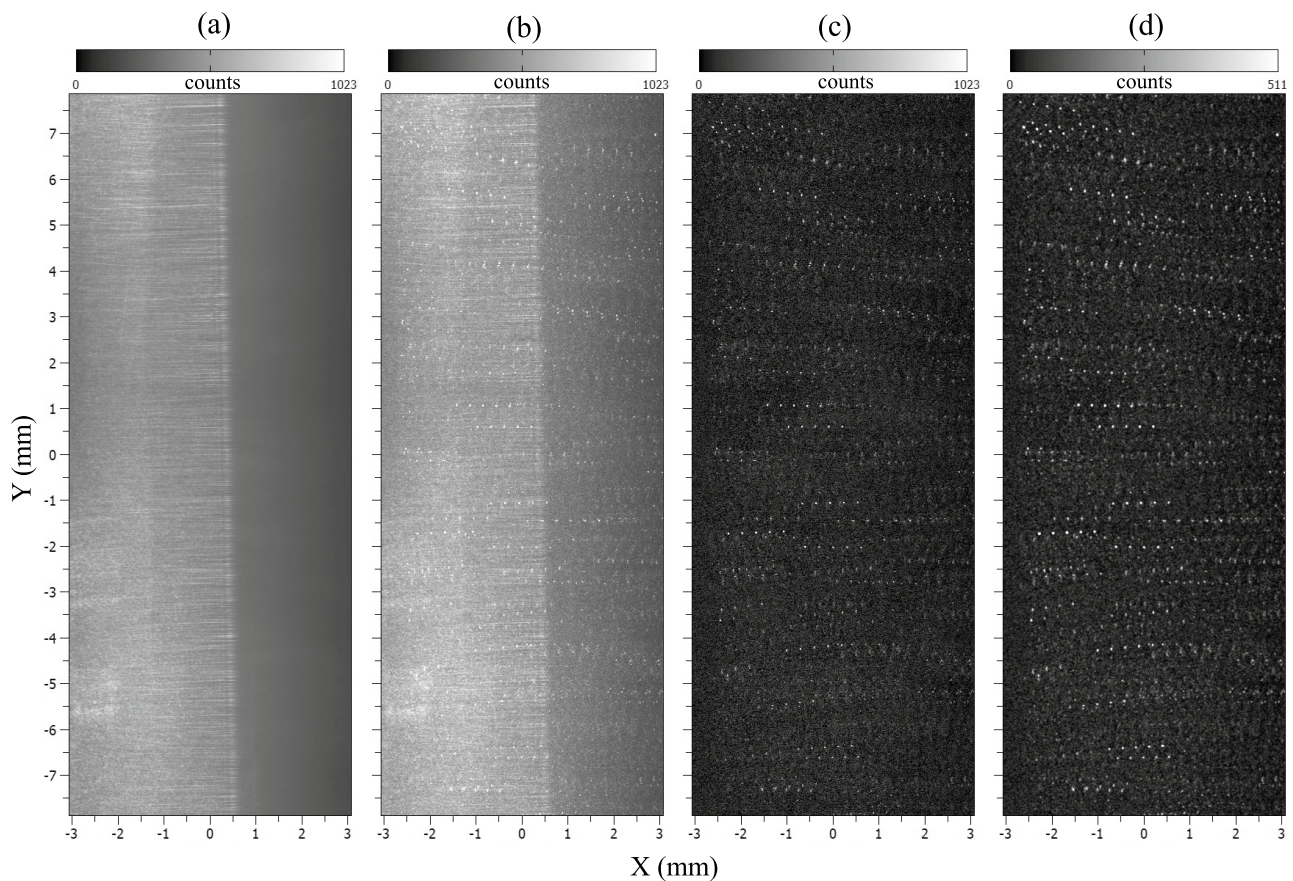


Fig. 13 Images data captured with a high-speed camera at 10 kHz for a turbulent flow in a square channel: mean intensity (a), raw, multi-exposed image (b), with mean subtracted (c), low-pass filtered (d). Five laser light pulses are overlaid

The correlation value in Fig. 17 is higher compared to Fig. 11 which is partly due to the reduced free stream velocity, approximately 3 ms^{-1} instead of 15 ms^{-1} . However, an improved seeding application was also tested using two seeding devices simultaneously (Seika CTS-1000 with dual flow nozzles and PIVTEC with standard Laskin nozzles). This comparison shows that the optimization of the seeding density, combined with a lower free stream airspeed, played a major role in enhancing the correlation value in the wake region for the selected recording parameters.

2.3.2 Wind tunnel test with laser illumination

In this setup, the light trap configuration between the imaging lens and the camera sensor was tested using a double-pulse PIV laser (Quantel Q-Smart, $\lambda = 532 \text{ nm}$) with a pulse separation of $20 \mu\text{s}$ as the light source. The laser was operated in Q-switched mode with a large flash lamp-to-Q-switch delay, reducing the light output to a small fraction of its usual design output of up to 380 mJ per pulse. The actual pulse energy was estimated using a Gentec laser power meter and is approximately in the range from 0.28 mJ to

0.55 mJ, although the measurement does not give an accurate or reliable result due to the very small energy levels. The collimated laser beam was expanded through a series of concave laser-grade lenses, rather than a standard camera lens, forming a diverging cone in the test section. The experiment was carried out in the one-meter wind tunnel (1 MG) at DLR Göttingen, which provided a uniform flow over the measurement area with a free-stream velocity of 8 ms^{-1} . Water droplets with a diameter of about $D_p = 2 - 3 \mu\text{m}$ were provided by a custom-built DLR generator. Due to the short lifetime of the water-based particles, the outlet of the seeding generator was placed just upstream of the cylinder test object, unfortunately causing some turbulent disturbances to the inflow. Again, the pco.edge 5.5 camera was used and the system operated at a frame rate of 9 Hz. The imaging lens was a Zeiss $f = 100 \text{ mm}$ lens set to an aperture of $f_{\#} = 2.0$. Figure 18 shows an example raw image (a) and the corresponding high-pass filtered image (b).

The image width is about 130 mm, almost four times wider than the setups with converging illumination as in Fig. 10. Unfortunately, the illumination is less homogeneous than in the previous tests with LED illumination. The

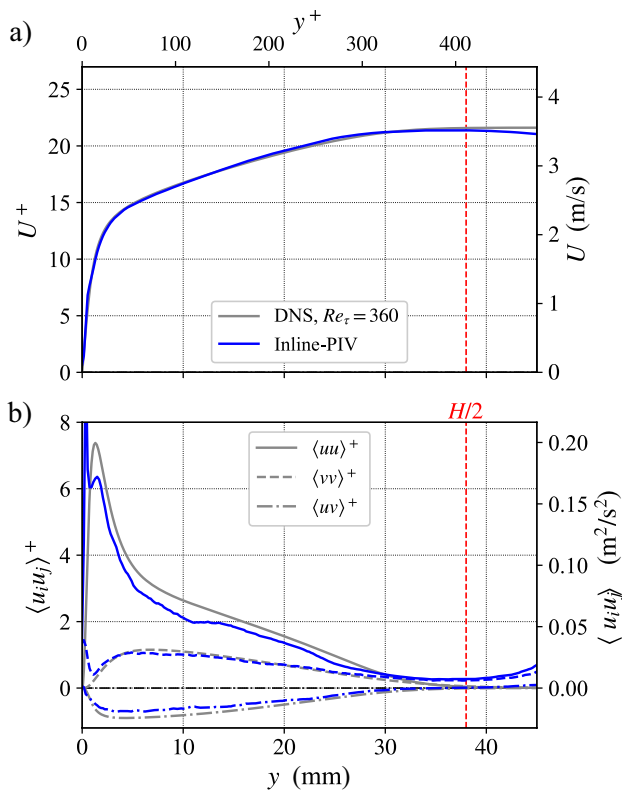


Fig. 14 Velocity profile (a) and variances (b) obtained with high-speed in-line PIV in a turbulent channel flow for a sampling rate of 20 kHz. DNS data from Schlatter and Örlü (2010). Red dashed line indicates channel centerline at $y/H = 0.5$

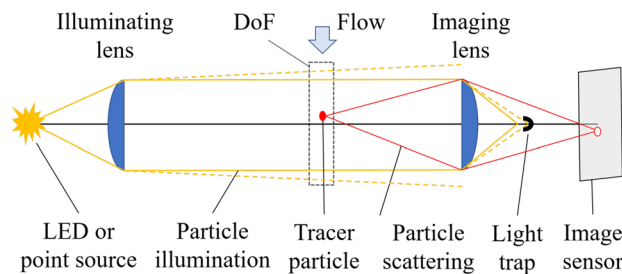


Fig. 15 Sketch of an in-line setup with a light trap between imaging lens and camera sensor, “configuration B”

main problem with the laser source was that it inadvertently created a laser speckle pattern that did not move with the local flow. The resulting horizontal velocity distribution after cross correlation analysis, see Fig. 19a, reflects the true velocity field only in the vicinity of the cylinder, see the yellow-red area. Further away from the cylinder, the result is erroneous at zero velocity (blue area) due to the stationary speckle pattern. Interestingly, the correlation coefficient of this pattern is even larger compared to tracer particle dominated areas with correct velocity measurements,

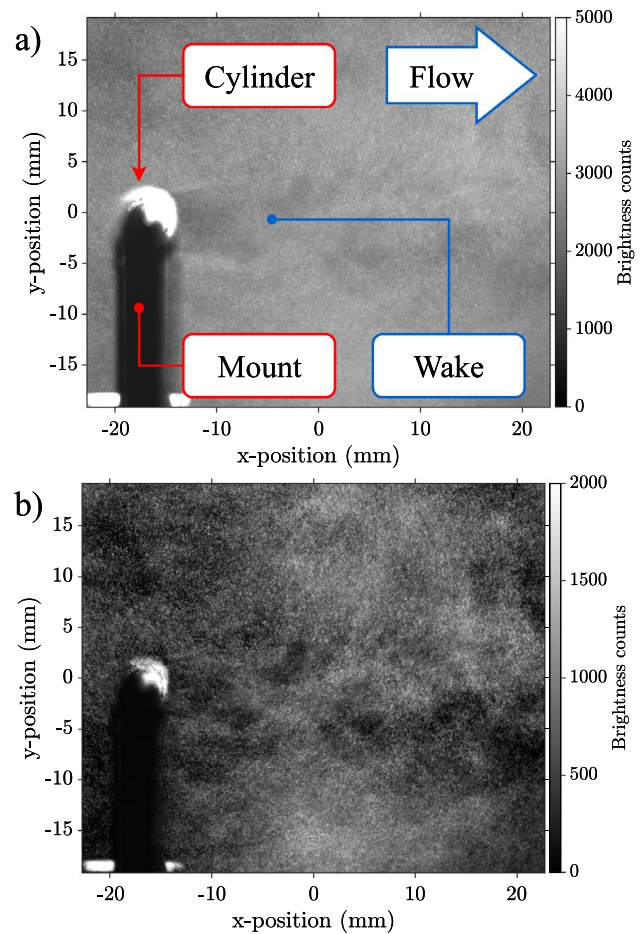


Fig. 16 Sample in-line PIV image with pulsed LED illumination, light trap behind the imaging lens, raw image (a) and high-pass filtered image (b)

see Fig. 19b. Nevertheless, it can be concluded that useful images can be obtained with such a setup, at least for some applications.

2.4 Setup with multiple light traps behind the illuminating lens

The previous setup with a light trap between the imaging lens and the image sensor requires very careful and delicate adjustment of the trap in relation to the other optical components. This is particularly true for laser illumination and long observation distances, as the focal point on the trap is close to the image plane and can easily damage the sensor.

2.4.1 Wind tunnel test with laser illumination and light trap on the illuminating side

A much more robust setup can be achieved by placing the light trap right behind the illuminating lens, see Fig. 20. In this case, the diverging illumination and the light trap

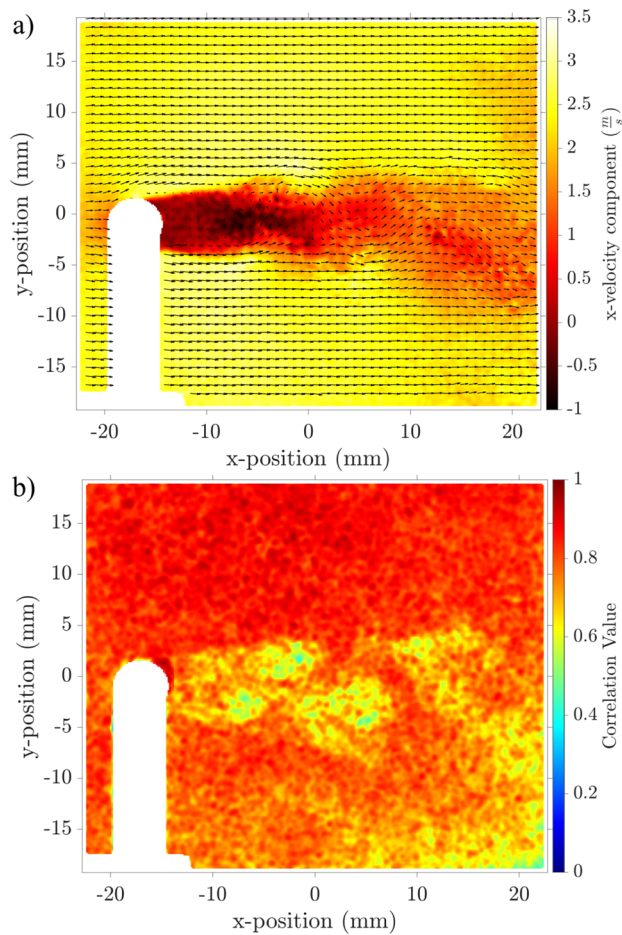


Fig. 17 Sample result for the raw image in Fig. 16, u-component velocity field (a, with every 6th vector in horizontal/vertical direction) and corresponding correlation coefficient (b)

create a diverging shadow that must cover at least the entire aperture of the imaging lens to prevent direct light from reaching the image sensor. Of course, this also leaves a shadowed area in the center of the measurement area. Light scattered by tracer particles outside this shadowed area can still be imaged by the camera. The ratio of the shadowed area to the illuminated area depends on the optical setup, such as the angle of divergence of the light cone and the focal length of the imaging lens. In practice, the shadow of the trap will not perfectly block the incident light, partly due to diffraction effects at the edge of the trap, which creates a bright corona. In an iterative process, it was found that stray light could be reduced by placing an additional light trap along the optical axis and in front of the imaging lens. Wind tunnel tests with this light trap configuration were carried out with an otherwise identical setup as in the previous section, Sect. 2.3.2. The two sub-figures of Fig. 21 respectively show an example image

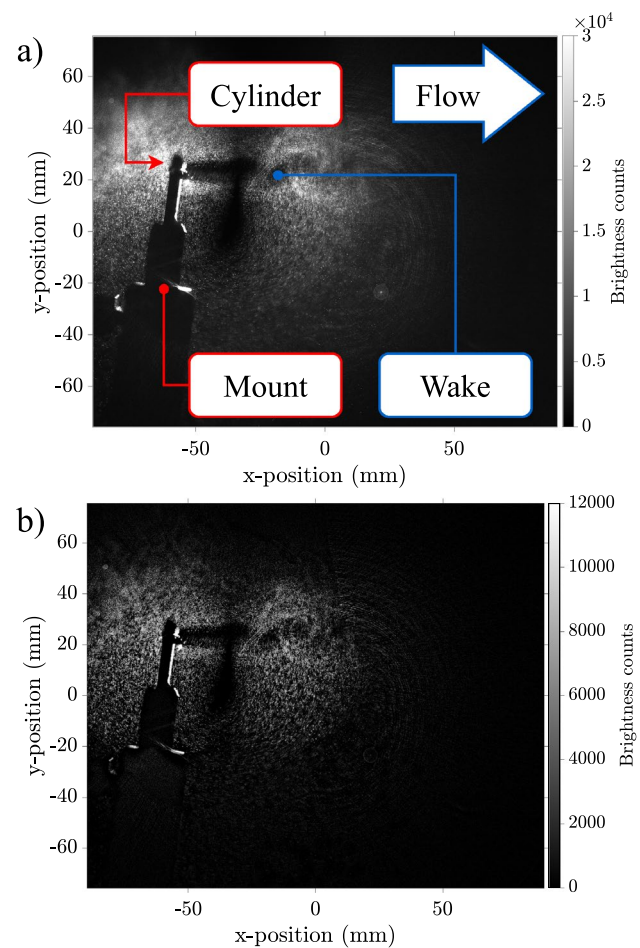


Fig. 18 Sample in-line PIV image with pulsed laser illumination, light trap behind the imaging lens, raw image (a) and high-pass filtered image (b)

before and after application of a high-pass filter. Compared to the previous setup (Fig. 18), the shadow of the light trap is visible as a dark area, indicated by a yellow circle. The cylinder itself is smaller, as indicated by the red circle.

The cross-correlation result is shown in Fig. 22 by means of the horizontal velocity component as a scalar background (a) and the correlation coefficient (b). The field of view is about 160 mm wide, and the seeded area is visible by a correlation coefficient with values around 0.5 (yellow-green area). With this setup, less laser speckles were generated, resulting in low correlation values outside the seeded area (dark blue areas). The trap shadow and cylinder mount have been masked out and appear as white areas. The velocity data is affected by some outliers that were not removed by post-processing, but the low velocity cylinder wake can be clearly seen as a horizontal red line in the right half of the velocity field.

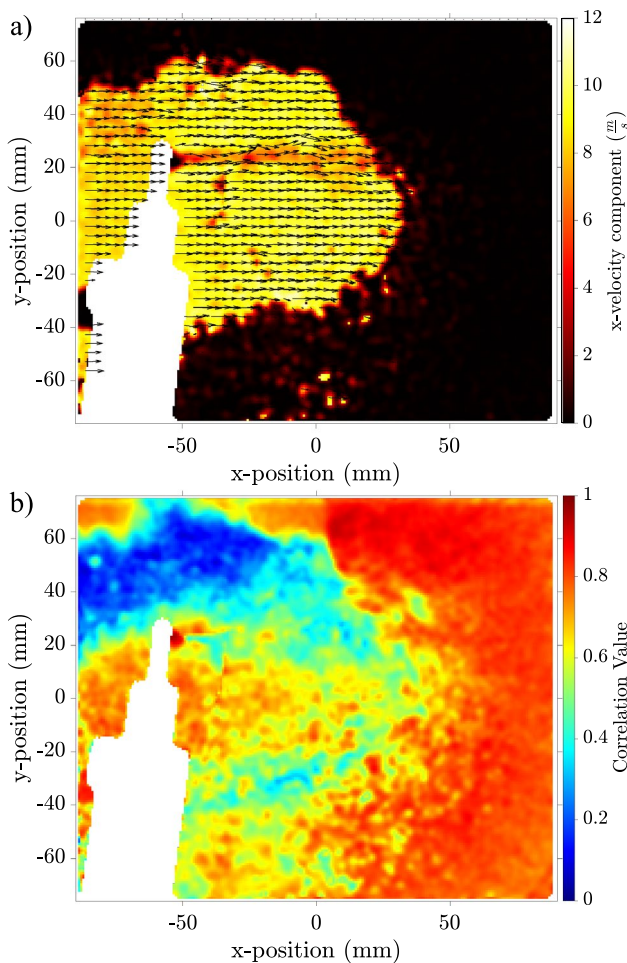


Fig. 19 Sample result for the raw image in Fig. 18, u-component velocity field (a, with every 6th vector in horizontal/vertical direction) and corresponding correlation coefficient (b)

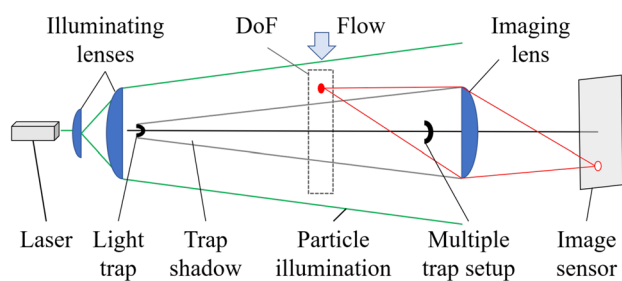


Fig. 20 Sketch of an in-line setup with a light trap behind the illuminating lens, “configuration C”

2.5 Alternative methods which benefit from high light efficiency

In contrast to the in-line PIV applications described above, we will now focus on two applications that used particle tracking instead of cross-correlation evaluation schemes.

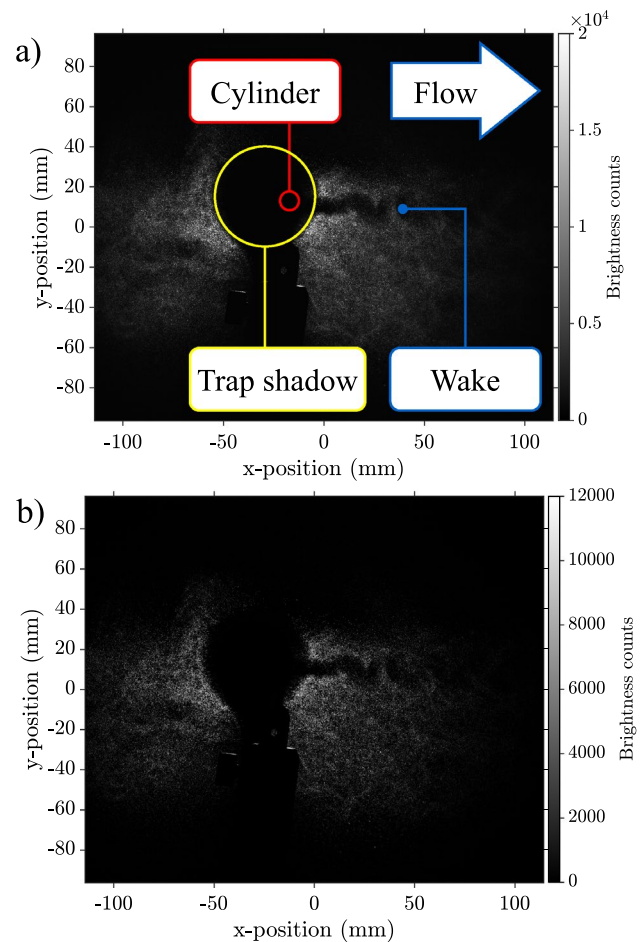


Fig. 21 Sample in-line PIV image with pulsed laser illumination, light trap behind the illumination lens, raw image (a) and high-pass filtered image (b)

One uses the relatively new technique of event-based image recording. The other uses a multiple aperture mask that acts as light trap at the same time. Both setups have the light trap in front of the imaging lenses as outlined in Sect. 2.2.

2.5.1 Bluff-body flow with laser illumination and event camera

Unlike conventional frame-based cameras, event cameras only capture intensity changes rather than the intensity itself. Aside from their high dynamic range (> 110 dB), the major advantage is that the data stream is reduced to transmitting only the pixels which observed a contrast change. This enables cost-effective high-speed imaging for a variety of applications (Gallego et al. 2022). The use of event cameras in PIV-like flow diagnostics is discussed by Willert and Klinner (2022), and Willert (2023). The primary motivation for use of an event camera in the present study was to assess

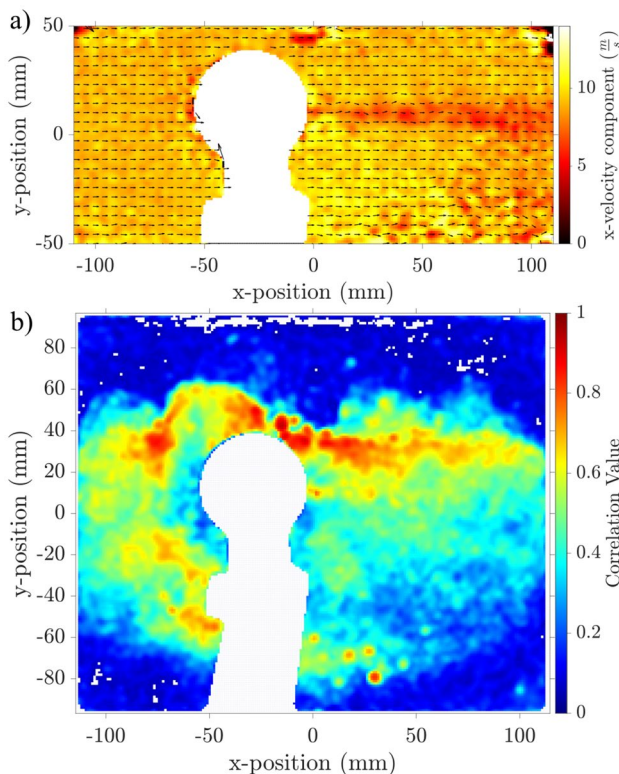


Fig. 22 Sample result for the raw image in Fig. 21, u-component velocity field (a, with every 6th vector in horizontal/vertical direction) and corresponding correlation coefficient (b)

whether in-line imaging arrangements provide sufficient intensity contrast to trigger contrast change events.

For the in-line setup shown in Fig. 7, an event camera with a resolution of 1280×720 pixels (Prophesee EVK2-Gen4.1) is combined with pulsed laser illumination. The same laser as in Sect. 2.2.2 is operated at a frequency of 5 kHz with a duty cycle of 1 – 2%. A neutral density filter with a transmission of 25% in the optical path results in single pulse energies of 2.5–6.2 μJ that are spread into a round beam of about 35 mm diameter in the measurement domain. The system is set up to image the seeded flow issuing from a 50 mm pipe using a $f = 300$ mm imaging lens with its aperture set at $f_{\#}4.0$. Seeding is provided paraffin tracer droplets of $D_p = 0.8 \mu\text{m}$ dispersed by a Laskin nozzle seeding generator (PIVTEC PivPart14). A 3 mm rod placed across the exit of the pipe provides a generic wake flow. The working distance between camera lens and measurement domain is about 500 mm. The DoF is estimated at 1–2 mm using the expressions given in the appendix.

Processing of the acquired event-streams using particle tracking algorithms reveals the path lines of individual particles in the wake of the cylinder wake flow (Fig. 23). The path-lines are shown as dashed traces, with the color indicating the corresponding particle velocity. The results clearly

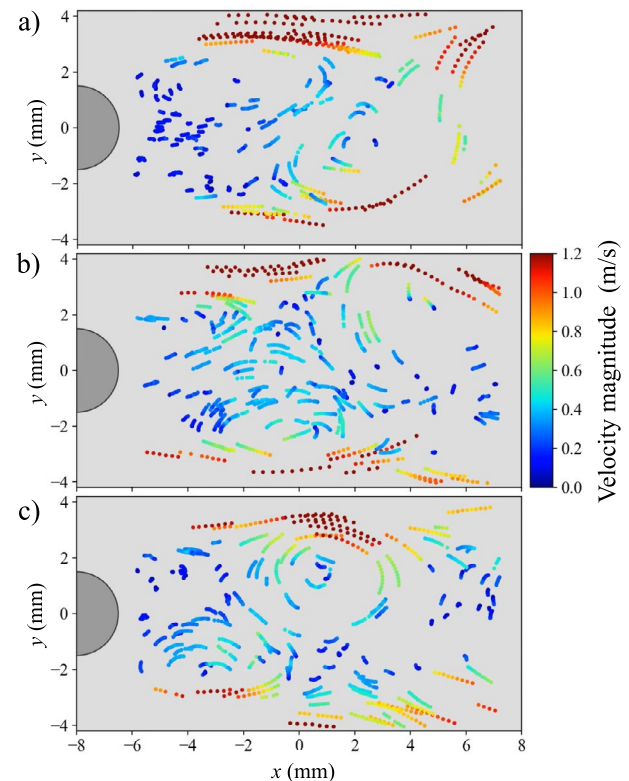


Fig. 23 Sample results for in-line PIV with an event-based camera showing pathlines of tracer particles, the coloring shows the corresponding particle velocity

capture both the external flow outside the cylinder wake with a velocity of about 1 ms^{-1} as well as the slower wake flow with several large-scale vortices.

2.5.2 Multi-aperture imaging setup

Another variant of the setup in Fig. 12, first described by Willert and Gharib (1992) and commonly referred to as *aperture encoded imaging* is shown in Fig. 24. In this setup, the imaging lens is nearly completely covered by a light trap, with the blue laser illumination focused in the central part of the trap. The light scattered by the flow tracer particles enters the imaging lens through three small off-axis aperture holes arranged in a triangular pattern. Particles in the focal plane of the lens will form a single sharp particle image on the sensor plane. Due to the three aperture holes, a tracer particle outside of the focal plane will be imaged as a triplet of three individual, nearly focused particle images rather than as a single but blurry out-of-focus particle image. The result is similar to the superposition of three images taken with three individual pinhole cameras with a small angular offset. The geometric size of the triplets can be related to the distance of the tracer particle to the focal plane, and the pattern orientation indicates whether the particle is in behind

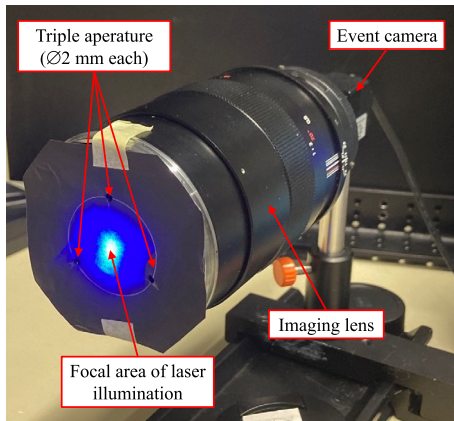


Fig. 24 Variant of a light trap in front of the imaging lens with three off-axis aperture holes

or in front of the focal plane (Willert and Gharib 1992). Combined with a spatial calibration, the system can be used to conduct three-component volumetric PTV measurements such as described by Pereira et al. (2000). To ensure a reliable detection of image triplets on the sensor plane, the number of particles that can be tracked at a given time is limited, resulting in a significant reduction of the spatial resolution in comparison to conventional PIV.

Figure 25 shows three samples of particle tracks recorded with an event-based camera using pulsed illumination. In the image, the tracer particles move from left to right. The tracer particle in track (a) is close to the focal plane, forming a triangle pointing to the left, whereas track (c) consists of larger triangular patterns facing the other direction indicating an increased distance from the focal plane. The switch in triangle orientation indicates that they are located on either side of the focal plane. Track (b) is produced by a particle moving within the focal plane. Figure 26 provides a close-up detail of a particle triplet track outside of the focal plane. The image also provides an impression of the

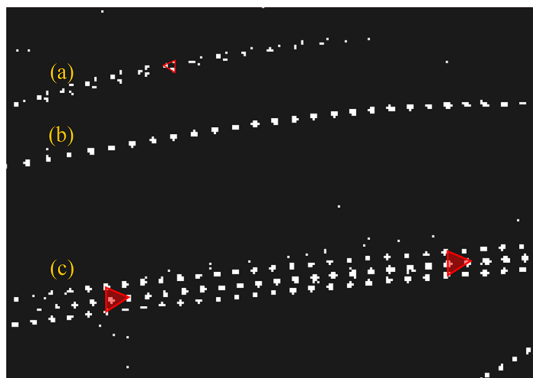


Fig. 25 In-line particle imaging with a triple-aperture light trap and pulsed laser illumination at 5 kHz (image width 440 pixel)

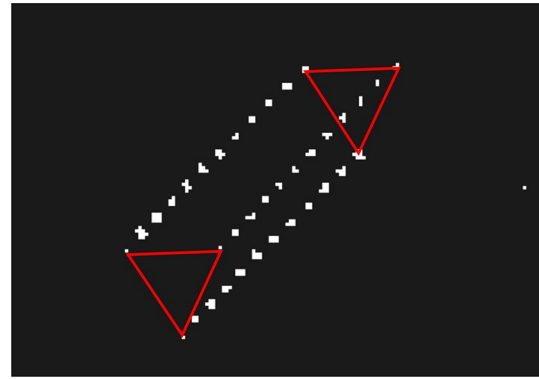


Fig. 26 Detail of a particle image track obtained for a particle outside of the focal plane using pulsed illumination at 5 kHz (12 pulses are shown, image width 220 pixel)

pixelated nature of the binary image data produced by the event-camera. It is noted that the triple-aperture setup itself is not directly related to the idea of in-line illumination. Nevertheless, it greatly benefits from in-line illumination, since a sufficient illumination intensity is provided despite the small pinhole-like aperture sizes.

3 Discussion

We tested various methods of in-line PIV recording and evaluation of which the most promising ones have been presented in this article and are summarized in Table 1. A pretest, that showed limited potential for macroscopic settings proved the feasibility of the in-line setup using two polarization filters. configuration A allowed for the recording of a transient flow with a limited field of view (FoV) due to the converging light cone. However, since small spherical particles do not alter the polarization direction of the scattered light, the polarization approach is limited to applications that allow for either larger or non-spherical particles. In configuration B the limited FoV was avoided by using a diverging light cone, but this exposed the recordings to imperfections of the imaging and illuminating lenses. Better results could be obtained with LED illumination in a controlled environment, and this configuration was then tested in the wind tunnel with a low-power laser. Since configuration B required careful positioning of the light trap between the imaging lens and the image sensor, a task critical for setups using laser illumination and long observation distances, the next step was to construct a more robust setup (configuration C in Table 1) with a double light trap. All alignments had to be done very carefully, as the proximity of the focal point to the image plane increased the risk of sensor damage. Another problem associated with this setup was the presence of the light trap shadow on the images. The first variation of configuration A mirrored the previous setup,

Table 1 Overview of the tested configurations

Configuration	Light source and number of light traps	Light trap position	Flow analyzed	Tracer	Observation
Polarization filter	Flashlight, no light trap but two polarization filters	Polarization filters with 90° offset	Uniform flow in a controlled environment	HSFB, $d \approx 300$ to $400 \mu\text{m}$	Used to show the validity of the approach
Config. A (see Sect. 2.2)	LED, one light trap	Light trap in front of the imaging lens	Cylinder wake in controlled environment	DEHS, $d \approx 1$ to $3 \mu\text{m}$	Proved the ability of recording an unsteady flow, FOV limited by converging light cone
Config. B (see Sect. 2.3)	LED/laser, one light trap	Light trap between the imaging lens and the camera's sensor	Cylinder wake in controlled environment (LED) and wind tunnel (laser)	DEHS, $d \approx 1$ - $3 \mu\text{m}$, solution of water and soap (unknown dimensions)	Overcame the limit on the FOV dimension by using a diverging light cone. However, the recording is very sensitive to lens imperfections. Better results were obtained with LED and the controlled environment
Config. C (see Sect. 2.4)	Laser, two light traps	One light trap on the side of the illuminating optics. The other one in front of the imaging lens (on both sides of the test section)	Cylinder wake in wind tunnel	Solution of water and soap (unknown dimensions)	Delicate adjustment of the light trap with regard to its position between the imaging lens and the image sensor, especially when using laser illumination and observing over long distances. Therefore, a more robust configuration with double light trap was built
Config. A V1 (see Sect. 2.2.2)	Laser, one light trap	In front of the imaging lens with a slight misalignment with respect to the camera's sensor	Duct flow	Paraffin droplets, $d \approx 1 \mu\text{m}$	Similar to the previous one but with low cost laser and in a small environment
Config. A V2 (see Sect. 2.5.1)	Laser, one light trap	In front of the imaging lens with a slight misalignment with respect to the camera's sensor	Bluff body with event-based camera	Paraffin droplets, $d \approx 1 \mu\text{m}$	The use of event-based camera allows to resolve a higher range of scale length
Config. A V3 (see Sect. 2.5.2)	Laser, one light trap	Light trap with three holes covering the imaging lens	Free particles in flow	Paraffin droplets, $d \approx 1 \mu\text{m}$	Combined with a spatial calibration, the system can be used to conduct three-component volumetric PIV measurements

but was used outside of the wind tunnel environment. The use of an event-based camera in this version extended our range of length scale resolution and demonstrated a considerable reduction of the required light intensity due to the increased sensitivity of the event-based sensor. Finally, a triple-aperture placed in front of the lens functioned as a light trap and produced self-similar image triplets on the sensor that allow a 3D reconstruction of particle in the imaged volume. Each configuration provided valuable insights into the nuances of our approach, offering distinct advantages and considerations. The set-ups shown were the ones that could be most easily realized. However, the maximum observation field size of some arrangements is restricted by aperture of the illuminating lens. Others demonstrated the feasibility of obtaining larger fields of view. The herein described in-line PIV techniques show potential for PIV measurements in open spaces, since they allow for the use of LED light sources instead of pulsed lasers, even when small tracer particles with diameters in the range of 1–3 μm are being used. The techniques worked best with high particle concentrations in the regime of the focal plane, but low particle concentrations in the surrounding area. Based on the configurations described in the previous sections several commonalities can be summarized:

- Tracer seeding within the imaging path, which are out of focus, will significantly reduce image contrast. Similarly, intermediate surfaces such as test section windows and lenses should be kept clean and scratch-free.
- For in-line imaging the depth of the measurement domain is defined by the DoF of the imaging lens. A combination of long focal length with large aperture and a considerable working distance can achieve a DoF in the millimeter range. For highly three-dimensional flows a limited depth of field requires the reduction of the separation time between both exposures to prevent loss of particle image pairing, just as in conventional PIV where the light sheet thickness defines the DoF.
- The in-line imaging arrangements have in common a relatively high background intensity level on which brighter particle images can be detected. Ideally this background is constant in time such that it can be removed through subtraction. For event-based imaging (c.f. Sect. 2.5.1), which relies on contrast changes, the difference between background and particle image has to be higher than the contrast detection threshold which typically is on the order of 20%.

4 Concluding remarks

Several configurations for in-line tracer particle illumination in seeded flows have been proposed and tested. The limited experimental results did not allow for a final rating, but

demonstrated feasibility and identified first characteristics enabling future investigations. The use of forward scattering has a significant influence on the required pulse energy of the light source used. Typically, sufficient illumination is achieved with about 1% of the pulse energy that would normally be used for a conventional orthogonal PIV arrangement employing a laser light sheet. It should be noted that the present work does not cover all possible configurations, nor have all aspects of this interesting technique been fully explored. Nonetheless, it can be concluded that for some experimental setups, both in gaseous and liquid media, interesting variations of the recording arrangement and along with reductions in the required light power can be achieved.

Appendix

Depth of field estimation

The depth of focus (DoF) for a given imaging setup depends on a number of parameters, in particular, the lens aperture (or f-number, $f_{\#}$), the focal length of the lens f , the working distance s and a quantity known as the circle of confusion or blur disk diameter d' . Related to these quantities is the magnification factor M which depends on the lens focal length f and working distance s .

Using the length of the Fraunhofer diffraction pattern d_f along the line of sight, Adrian (1991) provides the following expression:

$$\text{DoF}_d = 4\lambda f_{\#}^2 \left(1 + \frac{1}{M}\right)^2 \quad (2)$$

with λ being the wavelength of light. For macroscopic lenses or lenses with teleconverters operating at magnifications near unity ($0.1 \lesssim M \lesssim 1$), the effective f-number is given as $f_{\#, \text{eff.}} = f_{\#}(1 + M)$. This value needs to be used in Eq. 2.

Using geometrical optics an alternative approximation of DoF for macroscopic imaging is provided by Naumann and Schröder (1992) and is based on an acceptable amount of blur on the sensor known as *blur disk diameter*, d' :

$$\text{DoF}_g \approx 2d'f_{\#} \left(\frac{M+1}{M^2}\right) = 2d'f_{\#, \text{eff.}} \left(\frac{1}{M^2}\right). \quad (3)$$

Acknowledgements The authors gratefully acknowledge the support by Markus Krebs during our experimental work. Joachim Kliner provided valuable assistance in the estimation of the depth of focus for the described imaging configurations.

Author Contributions Markus Raffel, Johannes Braukmann, Christian Willert and Christian Wolf commonly developed the governing procedures and performed experiments. Luca Giuseppini continuously improved the procedure during the course of the experiments for his master thesis work in Göttingen. All authors commonly wrote the main

part of the manuscript in an iterative procedure and each of them prepared figures.

Funding Open Access funding enabled and organized by Projekt DEAL. The work was carried out and funded as part of the DLR project “URBAN Rescue”.

Data Availability The experimental data obtained for this study are accessible upon reasonable request, by contacting the corresponding author.

Declarations

Conflict of interest Not applicable. The authors declare no competing interests.

Ethical approval Not applicable.

Open Access This article is licensed under a Creative Commons Attribution 4.0 International License, which permits use, sharing, adaptation, distribution and reproduction in any medium or format, as long as you give appropriate credit to the original author(s) and the source, provide a link to the Creative Commons licence, and indicate if changes were made. The images or other third party material in this article are included in the article's Creative Commons licence, unless indicated otherwise in a credit line to the material. If material is not included in the article's Creative Commons licence and your intended use is not permitted by statutory regulation or exceeds the permitted use, you will need to obtain permission directly from the copyright holder. To view a copy of this licence, visit <http://creativecommons.org/licenses/by/4.0/>.

References

- Adrian RJ (1991) Particle-imaging techniques for experimental fluid mechanics. *Annu Rev Fluid Mech* 23(1):261–304. <https://doi.org/10.1146/annurev.fl.23.010191.001401>
- Bohren CF, Huffman DR (1998) Absorption and scattering by a sphere. John Wiley & Sons Ltd, chap 4:82–129. <https://doi.org/10.1002/9783527618156.ch4>
- Gallego G, Delbrück T, Orchard G et al (2022) Event-based vision: a survey. *IEEE Trans Pattern Anal Mach Intell* 44(1):154–180. <https://doi.org/10.1109/TPAMI.2020.3008413>
- Gao PF, Lei G, Huang CZ (2021) Dark-field microscopy: recent advances in accurate analysis and emerging applications. *Anal Chem* 93(11):4707–4726. <https://doi.org/10.1021/acs.analchem.0c04390>
- Huang WJ, and. Cai, Wu Y, Wu X, (2022) Recent advances and applications of digital holography in multiphase reactive/nonreactive flows: a review. *Meas Sci Technol*. <https://doi.org/10.1088/1361-6501/ac32ea>
- Jovanovic N, Martinache F, Guyon O et al (2015) The Subaru coronagraphic extreme adaptive optics system: enabling high-contrast imaging on solar-system scales. *Publ Astron Soc Pac* 127(955):890–910. <https://doi.org/10.1086/682989>
- Naumann H, Schröder G (1992) Bauelemente der Optik - Taschenbuch der technischen Optik, 6th edn. Carl Hanser Verlag, Vienna, Austria
- Pereira F, Gharib M, Dabiri D et al (2000) Defocusing digital particle image velocimetry: a 3-component 3-dimensional DPIV measurement technique. Application to bubbly flows. *Exp Fluids* 29(suppl 1):S078–S084. <https://doi.org/10.1007/s003480070010>
- Raffel M, Willert CE, Scarano F et al (2018) Particle image velocimetry: a practical guide. Springer, Cham. <https://doi.org/10.1007/978-3-319-68852-7>
- Renotte E, Alia A, Bemporad A, et al (2015) Design status of ASIICS, an externally occulted coronagraph for PROBA-3. In: SPIE Proc. Vol. 9604: solar physics and space weather instrumentation VI. SPIE, Bellingham, WA, USA, pp 1–15. <https://doi.org/10.1117/12.2186962>
- Rouan D, Riaud P, Boccaletti A et al (2000) The four-quadrant phase-mask coronagraph. i. principle. *Publ Astron Soc Pac* 112(777):1479–1486. <https://doi.org/10.1086/317707>
- Schardin H (1942) Die Schlierenverfahren und ihre Anwendungen. *Ergebnisse der exakten Naturwissenschaften* 20:303–439
- Schlatter P, Örlü R (2010) Assessment of direct numerical simulation data of turbulent boundary layers. *J Fluid Mech* 659:116–126. <https://doi.org/10.1017/S0022112010003113>
- Schwarz C, Bauknecht A, Wolf CC et al (2022) A full-scale rotor-wake investigation of a free-flying helicopter in ground effect using BOS and PIV. *J Am Helicopter Soc* 65(3):1–20. <https://doi.org/10.4050/JAHS.65.032007>
- Settles GS (2001) Schlieren and Shadowgraph Techniques, 1st edn. Springer International Publishing AG, Cham, Switzerland, doi: <https://doi.org/10.1007/978-3-642-56640-0>
- Wei N, You J, Friehs K et al (2007) In situ dark field microscopy on-line monitoring of yeast cultures. *Biotechnol Lett* 29(3):373–378. <https://doi.org/10.1007/s10529-006-9245-x>
- Willert C, Gharib M (1992) Three-dimensional particle imaging with a single camera. *Exp Fluids* 12:353–358
- Willert CE (2023) Event-based imaging velocimetry using pulsed illumination. *Exp Fluids* 64(98):1–19. <https://doi.org/10.1007/s00348-023-03641-8>
- Willert CE, Klinner J (2022) Event-based imaging velocimetry: an assessment of event-based cameras for the measurement of fluid flows. *Exp Fluids* 63(101):1–20. <https://doi.org/10.1007/s00348-022-03441-6>

Publisher's Note Springer Nature remains neutral with regard to jurisdictional claims in published maps and institutional affiliations.